

# Viscoplastic water entry

Maziyar Jalaal<sup>1,†</sup>, Dave Kemper<sup>1</sup> and Detlef Lohse<sup>1,2</sup>

<sup>1</sup>Physics of Fluids Group, Max Planck Center for Complex Fluid Dynamics, MESA+ Institute and J.M. Burgers Center for Fluid Dynamics, University of Twente, P.O. Box 217, 7500 AE Enschede, The Netherlands

<sup>2</sup>Max Planck Institute for Dynamics and Self-Organisation, 37077 Göttingen, Germany

(Received 4 September 2018; revised 1 November 2018; accepted 30 December 2018; first published online 11 February 2019)

The impact of viscoplastic droplets on a free surface of water is studied. The droplet undergoes an elasto-plastic deformation at the early stages of water entry. At large time, the yield stress dominates; therefore, the droplet solidifies and reaches an equilibrium shape. Depending on the impact velocity and the rheology of the droplet, the final morphologies vary from pear-shaped to capsules that contain bubbles. We perform an analysis of the orders of magnitude of the forces and introduce the relevant dimensionless groups. Furthermore, we categorize the final shapes in a phase diagram and analyse their geometrical properties. The process presents a method of making non-spherical beads and capsules with tunable shapes and provides information on the general problem of the impact of highly deformable objects on a liquid surface.

**Key words:** drops

---

## 1. Introduction

In the classical water-entry problem, a solid object passes through a water–air interface and forms an air cavity, which later retracts, resulting in the formation of a liquid jet. The problem has been extensively studied for more than a century since Worthington (1908), and the effects of the relevant physical parameters, such as density ratio, wettability and impact velocity, have been characterized (see Truscott, Epps & Belden (2014) for a review). The dynamics of water entry, however, differ when the deformability of the impacting object changes. A recent study on the impact of elastomeric spheres on water demonstrated that the deformation of the object upon impact and its consequent vibration notably change the shape of the air cavity (Hurd *et al.* 2017). In the same context, one can look at the impact of an immiscible droplet (e.g. water droplet on a bath of oil) as an ultimate case of water entry of highly deformable objects, where the capillary forces tend to keep the shape spherical. In such systems, the higher the inertia, the higher the deformation of the droplet, and, eventually, fragmentation can occur (Lhuissier *et al.* 2013). Note that, in comparison with the classic water-entry experiments, where the density of the impacting object

<sup>†</sup> Email addresses for correspondence: [m.jalaal@utwente.nl](mailto:m.jalaal@utwente.nl), [mazi@alumni.ubc.ca](mailto:mazi@alumni.ubc.ca)

is much larger than the density of the liquid bath (e.g. steel ball impacting water), a liquid–liquid system typically features a smaller impactor, a lower density ratio, and therefore a smaller impact momentum.

In the present study, we investigate the water entry of a viscoplastic (also known as yield stress) object. Such a material, if not sufficiently stressed, behaves like an elastic solid, but once the stress exceeds a critical value (the yield stress), the material deforms like a viscous fluid (typically with a nonlinear viscosity). Yield stress is a common property in many of the materials we deal with on a daily basis, such as toothpaste, cosmetic creams or muds. Besides, several industrial fluids such as waxy oil feature this property (see Balmforth, Frigaard & Ovarlez (2014), Coussot (2014) and Bonn *et al.* (2017) for reviews). A few studies have previously investigated the impact and spreading of viscoplastic droplets on a solid surface. It is shown that yield stress can prohibit the recoil of the droplet, retard the deformation after the drop has reached the maximum shape, and prevent splashing (German & Bertola 2009; Luu & Forterre 2009; Jalaal & Stoeber 2014; Blackwell *et al.* 2015; Jalaal, Balmforth & Stoeber 2015; Jalaal 2016; Jalaal *et al.* 2018).

The present scenario offers a version of a water-entry problem, in a sense that an initially solid material passes through an air–water interface. The system, nevertheless, diverges from classical water-entry experiments in some ways. We expect that the complex rheological properties of the soft impacting object change the dynamics of the entry. First, if the stress due to the impact is larger than the yield stress, the drop might undergo a (local or global) deformation, which in turn can change the dynamics of the cavity. Second, the density of the impacting object is higher for the majority of previous water-entry experiments (also see Truscott, Epps & Techet 2012). In comparison to the impact of immiscible droplets onto a water bath, the solid-like properties of the impacting object, i.e. yield stress and elasticity, as well as the shear-rate-dependent viscosity, alter the dissipation mechanism during the impact. Furthermore, we expect a static droplet shape when the exerted stress is below the yield stress everywhere inside the droplet.

Regarding applications, the subject of this work is directly relevant to the production of capsules, beads and non-spherical particles (see e.g. Wang *et al.* 1997; Beesabathuni *et al.* 2015; Lee, Beesabathuni & Shen 2015) where droplets polymerize, passing through a liquid–air interface. Apart from its possible direct applications, the current study might give a broader perspective on the general physics of impact and penetration of deformable objects that undergo elasto-plastic deformations (Lush 1983; Peseux, Gornet & Donguy 2005).

The paper is organized as follows: in § 2, we provide information on the properties of the materials used and describe the experimental conditions; in § 3, we first explain the phenomena observed in the tests, followed by the force analysis and quantitative measurements; § 4 concludes the results.

## 2. Experiments

### 2.1. Viscoplastic fluids

For our experiments, we used a mixture of Milli-Q water and a commercial hair gel at five different concentrations. The polymeric solution is essentially an aqueous mixture of Carbopol that is pH-neutralized with triethanolamine (see Dinkgreve *et al.* 2016). To increase the visibility of the droplets during the recordings, a small quantity (0.02 wt%) of ink (Trypan Blue by Sigma) is added to the solution. Finally, the samples are centrifuged at 2000 r.p.m. for 5 min to obtain a homogeneous mixture

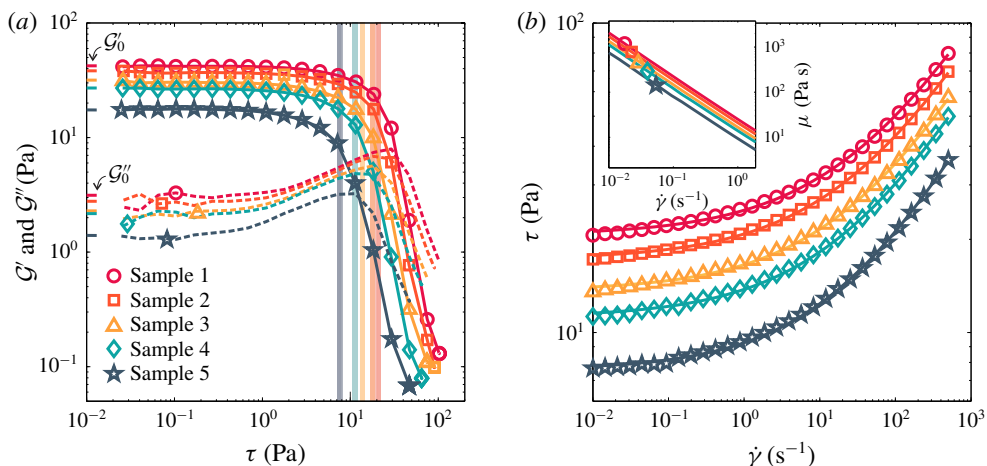


FIGURE 1. (Colour online) (a) The results of the oscillatory shear tests: symbols connected with lines correspond to storage ( $\mathcal{G}'$ ), and the dashed lines correspond to the loss ( $\mathcal{G}''$ ) moduli, respectively. The symbols denote the measurements for the samples listed in the legend. The polymer concentration decreases from sample 1 to 5. The vertical lines refer to the values of the yield stress,  $\tau_0$ , from Herschel–Bulkley (HB) fits. The magnitudes of  $\mathcal{G}'_0$  and  $\mathcal{G}''_0$  are shown on the y-axis. (b) Flow curves from the  $\dot{\gamma}$ , shear-rate-controlled, tests: the symbols are the same as in panel (a). The lines correspond to the HB fits (2.1). The inset shows the values of the apparent viscosity at low stresses.

without bubbles. We performed the rheological measurements using a rotational Anton Paar rheometer (MCR 502) with a cone-and-plate configuration ( $2^\circ$  angle and mean gap of 1 mm). Rough surfaces were used in the measurements to avoid slip effects at low shear rates (Roberts & Barnes 2001). First, we performed the oscillatory tests for a range of shear stresses (roughly 0.03 Pa–100 Pa) at the fixed frequency of 1 Hz to identify the storage ( $\mathcal{G}'$ ) and loss ( $\mathcal{G}''$ ) moduli. The values of  $\mathcal{G}'$  and  $\mathcal{G}''$  were independent of the oscillation frequency within the range of 0.1–10 Hz. Second, we obtained the steady-state flow curves of the materials in shear-rate-controlled ( $\dot{\gamma}$ -controlled) experiments, where the samples were initially pre-sheared for 2 min in an upward ramp of  $10^{-2} \text{ s}^{-1} < \dot{\gamma} < 500 \text{ s}^{-1}$ . Thereafter, the stress was measured in a downward ramp in the same range. The flow curves were independent of waiting times longer than 1 s. No hysteresis was observed in the up and down shear-rate ramps, suggesting negligible thixotropy. Additionally, we repeated the rheology measurement over the course of several days of the experiments to confirm that the samples retain their properties throughout the experiments.

Figure 1 summarizes the rheology of the materials used in our experiments. The results of the oscillatory tests reveal an elastic-dominant behaviour at low stresses, where  $\mathcal{G}' \approx 10\mathcal{G}''$ . Above a certain stress, the values of the storage modulus drop by orders of magnitude. Meanwhile, the loss modulus initially increases, crosses the curves of the storage modulus and then sharply decreases. Such behaviour shows a transition at a critical stress, from an elastic solid-like material (with weak viscous properties) to an elasto-viscoplastic material (with weak elastic properties). The flow curves (figure 1b) display the characteristics of the materials above the critical stress. The samples feature a shear-thinning behaviour, i.e. the viscosity reduces with increasing shear rate. Moreover, the measured stress values approach the yield stress

Sample	$\tau_0$ (Pa)	$K$ (Pa s <sup><i>n</i></sup> )	$n$	$\mathcal{G}'_0$ (Pa)
1	20.63	4.20	0.424	41.89
2	17.24	3.58	0.430	36.53
3	13.64	2.92	0.434	30.42
4	11.20	2.58	0.434	26.63
5	7.87	1.70	0.426	17.61

TABLE 1. Values of yield stress ( $\tau_0$ ), consistency index ( $K$ ), flow index ( $n$ ) and storage modulus ( $\mathcal{G}'_0$ ), from (2.1).

when  $\dot{\gamma} \rightarrow 0$ . Consequently, the apparent viscosity diverges at this limit (see the inset in figure 1*b*). We use a simple elasto-viscoplastic constitutive model to characterize our samples:

$$\tau = \mathcal{G}'_0 \gamma \quad \text{if } \tau < \tau_0 \quad \text{and} \quad \tau = \tau_0 + K \dot{\gamma}^n \quad \text{if } \tau \geq \tau_0, \quad (2.1a,b)$$

where  $\gamma$  is the strain,  $\mathcal{G}'_0 = \mathcal{G}'(\tau \rightarrow 0)$ , and  $K$  and  $n$  are the consistency and flow indices, respectively. The model assumes the material to be a linear elastic solid, as long as the shear stress is below the yield stress. Otherwise, if the stress is above the yield stress, the material flows like a Herschel–Bulkley (HB) fluid (Herschel & Bulkley 1926; also see Saramito 2009). In (2.1), if  $n < 1$ , the fluid is shear thinning; if  $n > 1$ , the fluid is shear thickening. For  $\mathcal{G}'_0 = 0$  and  $n = 1$ , the model above reduces to a Bingham model (Bingham 1917), where, if  $\tau \geq \tau_0$ , the fluid flows with a constant plastic viscosity ( $\mu_p = K$ ). Note that equation (2.1) ignores the viscous contribution below the yield stress and does not include any elasticity above it (i.e. viscoelasticity).

The coefficients  $\tau_0$ ,  $K$ ,  $n$  and  $\mathcal{G}'_0$  are listed in table 1 for the fluids used in the experiments. The higher the concentration of the polymer, the higher the yield stress and the elastic storage modulus, i.e. the solid-like behaviour of the material is more pronounced and the required stress to result in yielding is higher. The value variation of the flow indices is nevertheless negligible. One can also compare the magnitude of the yield stress listed in table 1 with the values of stress at which the curves of  $\mathcal{G}'$  and  $\mathcal{G}''$  cross over (yet another technique to measure the yield stress). The vertical lines in the plot indicate the values of  $\tau_0$  from the HB fits. These values are slightly smaller than the ones where the curves of  $\mathcal{G}'$  and  $\mathcal{G}''$  cross. This is consistent with recent measurements of a similar type of viscoplastic fluid (Dinkgreve *et al.* 2016).

Recent work measuring the surface tension of Carbopol solutions found that its deviation from that of water was small (less than 10%) and that it did not vary strongly with polymer concentration (Manglik, Wasekar & Zhang 2001; Jørgensen *et al.* 2015). Here, we do not measure the surface tension ourselves and use the fiducial value of  $\sigma = 0.072 \text{ N m}^{-1}$  for both water and the gel. We measured the density of the solutions using an Anton Paar DMA-35 density meter. The density of the used water is  $998.3 \text{ kg m}^{-3}$ , and the density of the viscoplastic gels varied between  $1000.0$  and  $1002.0 \text{ kg m}^{-3}$ . Note that, although the gels are in essence miscible in water, the diffusion time scale is much larger than the time scale of our experiments, i.e.  $Pe = U_0 D_s / \mathcal{D} \ll 1$ , where  $Pe$  is the Péclet number,  $\mathcal{D}$  is the mass diffusion coefficient,  $U_0$  is the impact velocity, and  $D_s$  is a characteristic length scale of the order of magnitude of the diameter of the droplet. Hence, the droplets are effectively immiscible in the time frame considered here.

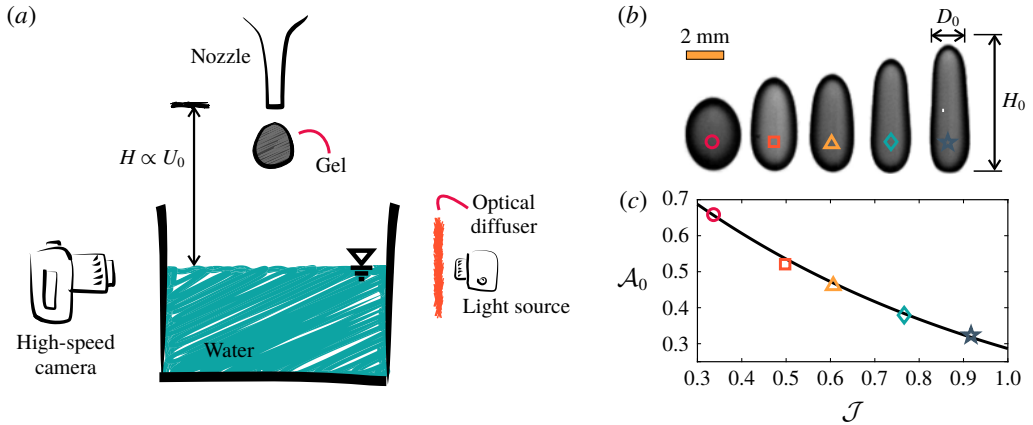


FIGURE 2. (Colour online) (a) Experimental set-up for the investigation of viscoplastic water entry. The shown dimensions are not to scale. (b) Shape of the droplets before impact for different gels (symbols are the same as in figure 1). (c) Variation of the aspect ratio versus  $\mathcal{J} = \tau_0 D_s / \sigma$ . The solid line is an empirical fit of  $\mathcal{A}_0 = e^{-1.25\mathcal{J}}$ .

## 2.2. Experimental set-up and initial shapes

Figure 2(a) shows a sketch of the set-up used for the impact test experiment. The drop of the viscoplastic fluid forms quasi-statically at the tip of a nozzle connected to a syringe pump. The inner and outer diameters of the nozzle are 1.15 mm and 1.65 mm, respectively. Droplets detach under their weight with a reproducible shape. The impact velocity is adjusted by varying the height of the nozzle and was measured just before the impact, using an image processing code. The bath, filled with Milli-Q water, is a cylindrical container with a diameter and height of 6 cm and 10 cm, respectively. The size of the bath is big enough such that it does not influence the impact process. The diffused light of the SLG-50S LED Fiber Optic Illuminator illuminates the water surface and a Photron FASTCAM SA-1.1 high-speed camera, connected to a Zeiss Milvus 100 mm  $f/2.0$  Macro-Planar T\* lens, records the process. The resolution of the images is set to  $1024 \times 1024$  pixels at a frame rate of 5000 frames per second and a shutter speed of  $8000 \text{ s}^{-1}$  to eliminate motion blur at high impact velocities. This results in a spatial resolution of  $\sim 64 \mu\text{m}$  in the air and  $\sim 54 \mu\text{m}$  in water. We correct the measurements for optical diffraction inside the container.

It was shown previously that the shape of a viscoplastic droplet detaching from a nozzle is mainly determined by the size of the nozzle, the yield stress and the surface tension (German & Bertola 2010). If the capillary pressure is much larger than the yield stress, the droplet will reach a spherical shape after the pinch-off. However, if the yield stress dominates, the droplet will become more prolate. Figure 2(b) illustrates the shape of the droplets for different gels. As expected, the larger the yield stress, the smaller the aspect ratio of the droplet ( $\mathcal{A}_0 = D_0/H_0$ ). For the fixed diameter of the nozzle, we characterize this geometrical parameter with a non-dimensional number  $\mathcal{J} = \tau_0 D_s / \sigma$ , where  $D_s = (6\mathcal{V}/\pi)^{1/3}$  is the diameter of a spherical droplet of the same volume,  $\mathcal{V}$ . The final results follow an empirical fit of  $\mathcal{A}_0 = e^{-1.25\mathcal{J}}$ . Note that the volume of the droplets for the range of the yield stresses we used do not vary, resulting in a constant value of  $D_s = 3.2 \pm 0.1 \text{ mm}$ .

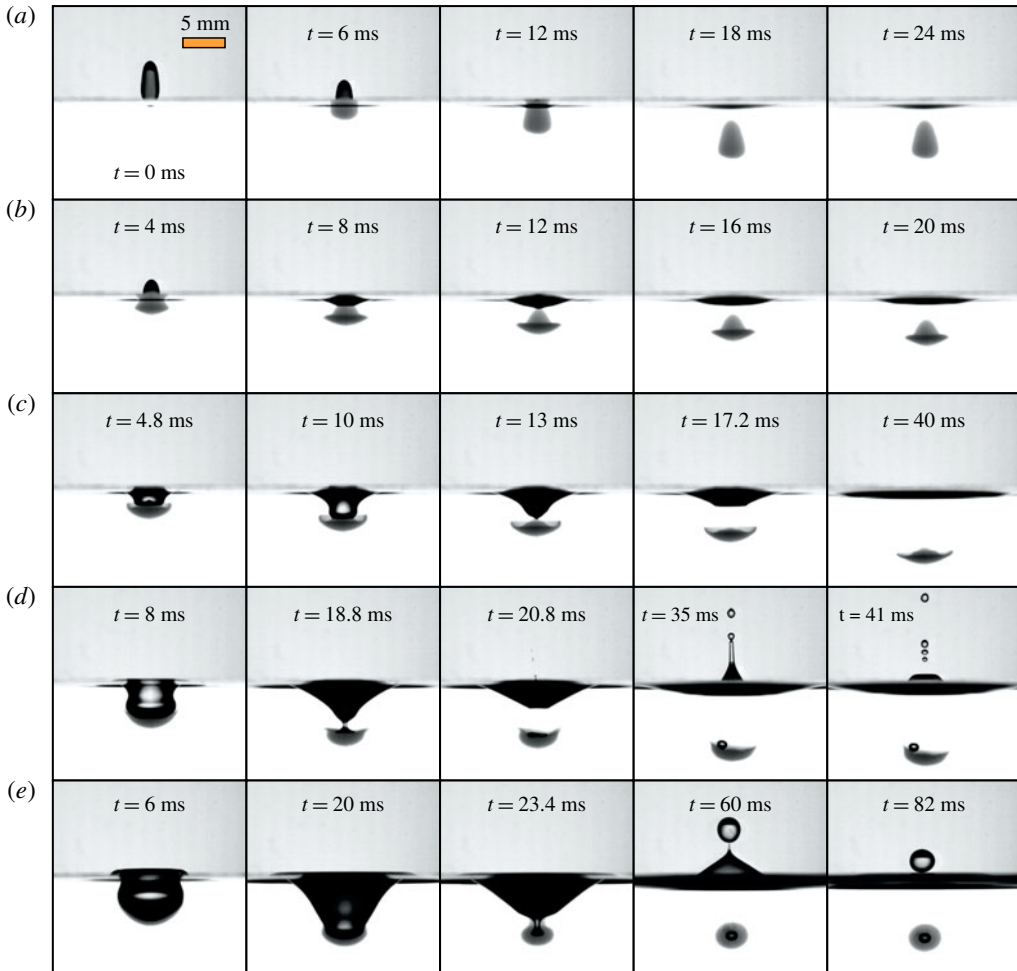


FIGURE 3. (Colour online) Water entry of a viscoplastic droplet (sample 3; see table 1 for the properties) at different impact velocities: (a)  $U_0 = 0.32 \text{ m s}^{-1}$  ( $\tau = D_s/U_0 = 10 \times 10^{-3}$ ); (b)  $U_0 = 0.72 \text{ m s}^{-1}$  ( $\tau = 4.44 \times 10^{-3}$ ); (c)  $U_0 = 1.12 \text{ m s}^{-1}$  ( $\tau = 2.86 \times 10^{-3}$ ); (d)  $U_0 = 1.41 \text{ m s}^{-1}$  ( $\tau = 2.27 \times 10^{-3}$ ); and (e)  $U_0 = 2.07 \text{ m s}^{-1}$  ( $\tau = 1.55 \times 10^{-3}$ ). See supplementary movies available at <https://doi.org/10.1017/jfm.2019.32>.

### 3. Results

#### 3.1. Phenomenology

This section outlines the qualitative mechanics of water entry of viscoplastic fluids. Figure 3 shows the entry of a droplet of sample 3 for a range of impact velocities  $0.32 < U_0 < 2.07 \text{ m s}^{-1}$ . At the lowest impact velocity shown (figure 3a, with  $U_0 = 0.32 \text{ m s}^{-1}$ ), the droplet undergoes a slight deformation, predominantly at the bottom, where it first hits the surface. The droplet rapidly reaches an equilibrium shape once it is fully submerged ( $t \approx 17 \text{ ms}$ , which corresponds to a non-dimensional time of  $t^* = U_0 t / D_s \approx 1.7$ ). In this regime, the comparison with the initial shape of the droplet reveals that the final shape features a flattened bottom and an unchanged top. This suggests that only the bottom of the droplet shears and experiences the

plastic deformation, while the top of the droplet falls freely. Here, we call such a morphology a pear shape. The elastic deformation in this regime is minimal and the size of the water cavity is small. Furthermore, after reaching an equilibrium shape, the droplet sinks in the bath because of the density difference. Hereafter, the dynamics is simply a solid-body falling motion. The falling motion of the droplets occasionally features fluttering or a rotating motion (not shown here), previously observed for falling non-spherical particles (e.g. Auguste, Magnaudet & Fabre 2013).

Figure 3(b) depicts the impact process at  $U_0 = 0.72 \text{ m s}^{-1}$ . Similar to figure 3(a), the majority of the deformation occurs at the early moments after the droplet touches the water surface ( $0 < t < 16 \text{ ms}$ ) and it affects only the bottom of the droplet. However, due to a higher impinging velocity, the stress on the droplet surface is higher and, consequently, the bottom of the droplet suffers more from plastic deformation. The top of the droplet does not deform, meaning it falls freely. We still call such a final morphology a pear-like shape, as long as the brims of the final shape are pointing downwards. Figure 3(c) shows the process of water entry at  $U_0 = 1.12 \text{ m s}^{-1}$ , where the further increase of the impact velocity results in more substantial deformation of the droplet. Again, the majority of the deformation occurs at the early stage of entry, and afterwards the droplet rapidly approaches a static shape. In comparison to figure 3(b), the brims are now larger, thinner and highly plastically deformed. Additionally, the depth of the air cavity at such speed is comparable to the size of the droplet. The cavity forms at the early stages of the droplet penetration and retracts while the droplet is still deforming. The retraction, however, does not lead to the formation of a Worthington jet. At this speed, one can also observe a late elastic deformation of the brims. After the droplet detaches from the cavity, it decelerates, the shear stress rapidly decreases, and therefore the thin brim bends back elastically (this can be seen by comparing the last two images in figure 3c). The elastic deformation leads to a larger equilibrium time,  $t \approx 35 \text{ ms}$  in this particular case. See appendix B for more quantitative details on the dynamics of the droplets and the cavities. We refer to this morphology as the sombrero shape, when the brim is facing upwards, and the tip of the peak in the middle of the droplet is higher than the tip of the brim. In some cases, the thin brim of the sombrero droplets is unstable and breaks due to the excessive shear stresses. The softer the gel, or the stronger the impact, the thinner the brim is, and consequently it is more likely to break.

Increasing the impact velocity at some point will lead to the formation of a bubble and a Worthington jet. Figure 3(d) shows the images of an impact at  $U_0 = 1.42 \text{ m s}^{-1}$ . At this velocity, the size of the cavity is larger, and it has a strong effect on the dynamics of the droplet. Initially, the droplet grows radially while the cavity expands. While retracting, the cavity and consequent flow inside the bath pull the droplet towards its centre. The cavity finally breaks into two parts. A large portion of the cavity that initially has a very sharp tip collapses and forms a Worthington jet that later disintegrates. The second part is an air bubble that initially sticks to the viscoplastic droplet (similar to the attached cavities in solid-body water entry). The bubble, however, detaches later on and stays above the droplet in the low-pressure wake zone. It finally rises to the surface of the bath (not shown here). The final shape of the droplet now looks like a bowl with a sharp edge. We refer to this morphology as a bowl-shaped droplet.

Further increase of the impacting momentum results in a surprising regime of bubble encapsulation (figure 3e). Similar to the previous regime, the droplet expands with the cavity. The breakup during the retraction, however, is different, where the

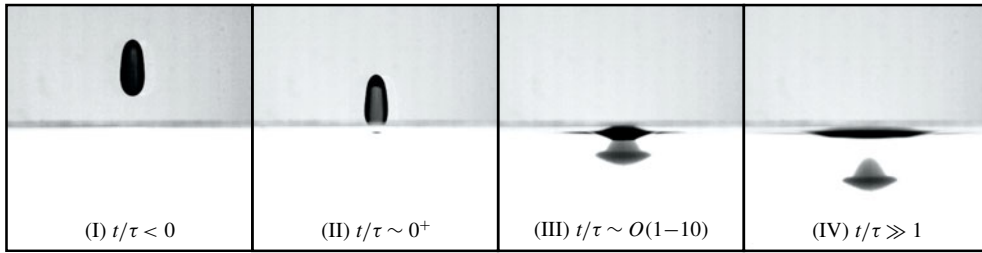


FIGURE 4. Four successive stages of the water entry from left to right. Here  $\tau = D/U_0$  is the inertial time scale. This example belongs to the same condition shown in figure 3(b).

location of the pinch-off is inside the viscoplastic droplet, and therefore bubble encapsulation occurs. Another observation is that, although inertia increases, the velocity of the jet formed above the surface significantly reduces and it only breaks into one large droplet. Further increase of the impacting velocity results in bubble encapsulation while the Worthington jet does not break up at all. The final shape of the droplet in this regime is close to a sphere and features a bubble inside: a capsule. Capsules sink slowly due to the buoyancy forces. Indeed, balancing the buoyancy and gravitational forces results in a critical bubble diameter of  $D_{bub} \approx (\frac{1}{2}D_{cap})^{1/3}$ , where  $D_{cap}$  is the capsule diameter, i.e. a capsule with a bubble larger than  $D_{bub}$  will rise. In our experiments, the size of the bubble is always slightly smaller than this value and therefore the capsules sink slowly.

### 3.2. Forces and non-dimensional numbers

Section 3.1 highlighted two distinct regimes. At low impact velocities, the influence of the cavity is minimal. By increasing the inertial effects, the size and the influence of the cavity become more pronounced, and bubble entrainment occurs. We inspect these two regimes separately, and compare our results to previous studies.

We look at the forces acting in the regime of low inertia (pears and sombreros) in four temporal stages, as shown in figure 4. Before the impact ( $t < 0$ ), the droplet is falling freely under gravity (stage I). Comparing the viscous drag forces in air ( $\sim \rho_{air} U_0^2 C_D D_s^2$ ) and the yield stress forces ( $\sim \tau_0 D_s^2$ ) results in a non-dimensional number of the form  $\mathcal{I}_Y = C_D^{-1} \tau_0 / \rho_{air} U_0^2$ . Prior to the impact, a typical value for the Reynolds number is  $Re = \rho_{air} U_0 D_s / \mu_{air} \sim O(100)$ , which results in a drag coefficient of  $C_D \sim O(1)$ . Therefore, we estimate  $\mathcal{I}_Y \sim O(10)$ , meaning that the shear stress forces are not strong enough to induce plastic deformation. For the same period, a comparison between the yield stress and the surface tension forces results in the number  $\mathcal{J} = \tau_0 D_s / \sigma$ . As previously discussed in § 2.2,  $\mathcal{J} \sim O(0.1-1)$ , meaning that the capillary action can be strong enough to deform the droplets. In our experiments, we have observed that the droplets slightly deform just after the pinch-off: the sharp tips (high-curvature regions) locally smooth and the droplet slightly retracts. Nonetheless, after a short time (which is much smaller than the falling time in all cases), the droplet reaches an equilibrium shape before impacting on the free surface (shown in figure 2b).

The early stages of the impact (stage II), i.e. the moment after the contact between the viscoplastic droplet and the water bath, can be associated with shock-type characteristics (Korobkin & Pukhnachov 1988). More complexities might also develop due to the effect of the air layer, as well as the elasto-plastic deformation of the

droplet. We do not address this regime in detail; nevertheless, in appendix A, we provide an analysis that manifests a pressure wave with a magnitude much larger than the yield stress at an effective time scale of  $\sim O(10^{-6}$  s). In our experiments, we do not see any particular deformation of the droplet as a consequence of such a pressure impulse.

Although the droplet decelerates in the early moments after it hits the surface, its velocity ( $U_d$ ) is still comparable with the impact velocity:  $0.1U_0 \lesssim U_d < U_0$  (also known for other impact and penetration problems (Yarin, Rubin & Roisman 1995; Berberović *et al.* 2009)). The penetration velocity at this stage results in a velocity gradient at the droplet–bath interface and hence an azimuthal vorticity (stage III in figure 4). In a classic Newtonian system, such vorticity typically leads to the emergence of vortex rings (see Thomson *et al.* 1886; Peck & Sigurdson 1994; Dooley *et al.* 1997; San Lee *et al.* 2015; Thoraval, Li & Thoroddsen 2016). For a viscoplastic droplet, the rollup deformation due to the vortex rings is not only damped due to the total viscosity, but also ceases when the yield stress dominates (also see appendix C). The moment the internal stress generated by the vortex motion is below the yield stress, the droplet approaches a final equilibrium shape. One can now follow the same calculation as above in air to obtain  $Re = \rho_{water}U_dD_s/\mu_{water} \sim O(100)$ , and  $C_D \sim O(1)$ . Accordingly,  $\mathcal{I}_Y \sim O(1)$ , i.e. at the initial moments of the submergence, the shear stress on the surface of the droplet is comparable to the yield stress and therefore enough to begin a plastic (and also elastic) deformation.

At stage IV ( $t \gg 1$ ), assuming a spherical shape, balancing weight ( $\sim \mathcal{V}\rho_{droplet}g$ ), buoyancy ( $\sim \mathcal{V}\rho_{water}g$ ) and drag ( $\sim \frac{1}{2}\rho_w U_f^2 C_D \pi R_s^2$ ) forces results in a terminal velocity of  $U_f = [\frac{4}{3}(gD_s/C_D)(\rho_D/\rho_w - 1)]^{0.5}$ . At this stage, considering the small density ratio ( $\rho_D/\rho_w \approx 0.002$ ), and assuming the viscous drag coefficient  $C_D = 24/Re$ , one finds a final velocity of  $U_f \sim O(10^{-3}$  m s $^{-1}$ ). Accordingly,  $\mathcal{I}_Y \sim O(10^4)$ . Additionally, the surface tension vanishes at this stage, hence,  $\mathcal{J} \sim 0$ . Therefore, long after crossing the air–water interface, the droplet retains its shape because of the yield stress and sinks slowly like a solid body.

The force analysis explained above for the low-impact-velocity regimes suggests that the majority of the deformation occurs from the moment of impact until shortly after the droplet is fully submerged (roughly  $0 < t/\tau < 10$ , where  $\tau = D_s/U_0$ ). In contrast, before impacting the surface ( $t/\tau < 0$ ) and sufficiently long enough after passing the interface ( $t/\tau \gg 1$ ), the droplet maintains its shape.

Stage III in the analysis above drastically changes at high impact velocities. For the regimes of bowl-shaped droplets and capsules, the air cavity plays a significant role in defining the final shape of the droplets. This is closely related to the well-studied phenomena of cavity formation and bubble entrainment (Bergmann *et al.* 2006, 2009; Peters, van der Meer & Gordillo 2013; Gielen *et al.* 2017). For the impact of a droplet on a bath of the same fluid, it is known that increasing the impact velocity leads to the formation of a cavity in the bath and wave swells at the free surface. For a narrow region of parameter space, the development of a moving capillary wave down the cavity wall results in bubble entrainment (Pumphrey, Crum & Bjørnø 1989; Oguz & Prosperetti 1990). In our case, the viscoplastic droplet spreads over the cavity while it grows. When the cavity stops, the different position of the free surface begins to retract with different speeds that eventually leads to the pinch-off of the tip and bubble entrainment. If the pinch-off occurs inside the droplet, capsules form. Balancing the capillary-wave time scale  $t_w \approx [8(\sigma/\rho)\kappa^3]^{-1/2}$ , where  $\kappa \approx 1/D_s$ , and the

time corresponding to the maximum crater depth,  $t_m \approx (D_s U_0^{1/3} \rho^{1/4}) / (64g\sigma)^{1/4}$ , yields

$$We \sim Fr^{1/5}, \quad \text{where} \quad We = \frac{\rho U_0^2 D_s}{\sigma} \quad \text{and} \quad Fr = \frac{U_0^2}{g D_s}. \quad (3.1a,b)$$

If the droplet spreads on the entire surface of the cavity, the cavity will grow perfectly radially and therefore no bubble will form in the retraction phase. Balancing the spreading diameter  $D_{sp} \approx D_s We$  (from the virtual mass force estimation) and the crater diameter  $D_c \approx D_s Fr^{1/4}$  (from the energy balance), we see that

$$We \sim Fr^{1/4}, \quad (3.2)$$

as the upper-bound scaling limit of the bubble entrainment regime for inviscid impacts. The scaling above agreed well with the experimental fits of  $We \sim Fr^{0.179}$  and  $We \sim Fr^{0.248}$ , for lower and upper limits, respectively (Oguz & Prosperetti 1990). Note that the prefactors in (3.1) and (3.2) are to be determined by experiments or numerical simulations. For an inviscid system, one expects a vortex-ring region below the lower limit, no bubble entrainment above the upper limit (Rein 1996) and bubble entrainment between the two.

Figure 5 compares our results with the results of Oguz & Prosperetti (1990) and a collection of other experimental data, some previously collected in Murphy *et al.* (2015). The inviscid bubble entrainment limits slightly underestimate the boundaries of bowls and capsules in our system, where bubbles form. This is consistent with the findings of Deng *et al.* (2007), who found that increasing the viscosity of the liquid weakens the capillary waves and shifts the limits: therefore, the higher the viscosity, the higher the impact velocity required to entrain a bubble. We anticipate that the presence of the viscoplastic layer at the free surface, during the retraction of the cavity, results in the same trend.

### 3.3. Phase diagram and final shapes

To classify the final morphologies of the viscoplastic droplets, we introduce a Reynolds number of the form

$$Re = \frac{\rho U_0^2}{K(U_0/D_s)^n + \tau_0}. \quad (3.3)$$

The number above compares the inertial stress and the total internal stress, which contains two parts due to the power law and the plastic viscosities. By using this non-dimensional group, we assume that the yield stress only contributes to the final shape via the plastic viscosity. A Reynolds number of this type has previously been used in the context of viscoplastic droplets (Blackwell *et al.* 2015) and other configurations (Thompson & Soares 2016; Liu & de Bruyn 2018) (also see Madlener, Frey & Ciezki 2009; Chen & Bertola 2017). In our experiments, except at very low impact velocities, the stress due to the inertia ( $\rho U_0^2 \sim O(10^2-10^4)$ ) is at least an order of magnitude larger than the viscous stresses ( $20 \lesssim K(U_0/D_s)^n \lesssim 70$ , and  $7 \lesssim \tau_0 \lesssim 20$ ). Beside the Reynolds number, we can choose either the Weber or the Froude number (see (3.1)), because our equivalent diameter,  $D_s$ , is fixed and therefore  $Fr = We/Bo$ , where  $Bo = \rho g D_s^2 / \sigma \approx 1.4$  in all cases. We categorize the final shape of the droplets in a phase diagram. Figure 6 shows the map of the final shapes in the  $Fr-Re$  space. At small  $Re$  and  $Fr$ , when inertial forces are not much stronger than the viscous stresses, and the

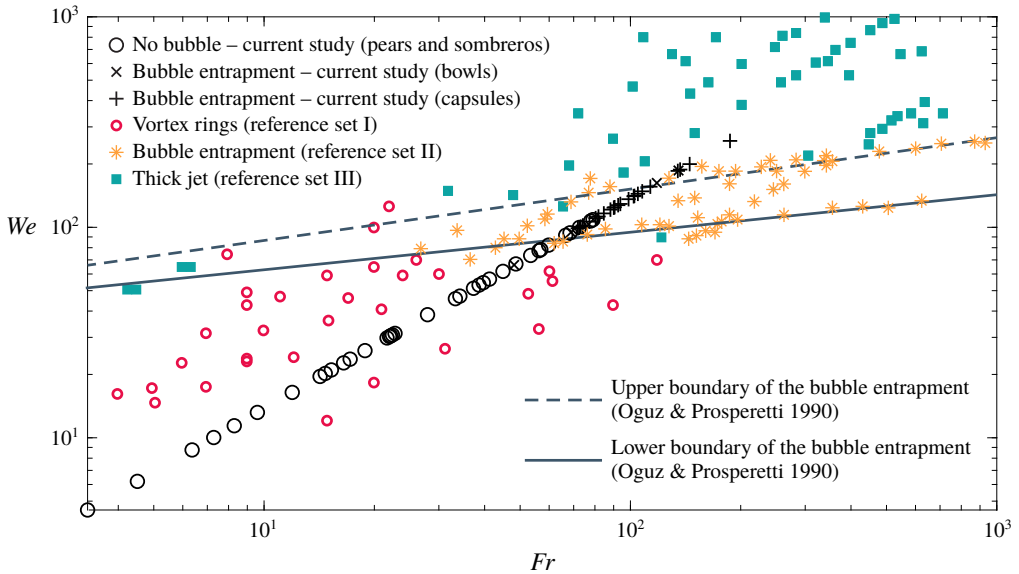


FIGURE 5. (Colour online) A  $We$ - $Fr$  plot showing the different behaviour upon impact of a droplet onto a bath. Reference set I: Chapman & Critchlow (1967), Esmailzadeh & Mesler (1986), Cai (1989), Pumphrey & Elmore (1990), Sigler & Mesler (1990), Rein (1996), Elmore, Chahine & Oguz (2001), Leng (2001), Deng, Anilkumar & Wang (2007) and Liow & Cole (2009). Reference set II: Pumphrey & Elmore (1990), Rein (1996), Morton, Rudman & Jong-Leng (2000), Elmore *et al.* (2001), Leng (2001), Deng *et al.* (2007) and Liow & Cole (2009). Reference set III: Worthington (1883, 1908), Franz (1959), Van de Sande, Smith & Van Oord (1974), Macklin & Metaxas (1976), Hallett & Christensen (1984), Hsiao, Lichter & Quintero (1988), Khaleeq-ur Rahman & Saunders (1988), Cai (1989), Pumphrey & Elmore (1990), Rein (1996), Morton *et al.* (2000), Fedorchenko & Wang (2004), Tomita, Saito & Ganbara (2007) and Bisighini *et al.* (2010).

cavities are small, the droplet deforms only at the bottom, and the final morphologies are pear-shaped. By increasing  $Re$  and  $Fr$  (i.e. inertial effects), the shapes transit to sombreros and bowls. Eventually, at sufficiently large  $Re$  and  $Fr$ , the capsules are formed. Figure 6 also highlights the boundaries in which the Worthington jet is formed (dashed line) and damped (dashed-dotted line). In between these two boundaries, a jet always forms and breaks up into one or multiple droplets due to the Rayleigh-Plateau instability.

We elaborate on the geometrical characteristics of the final shapes, measuring the final aspect ratio of the droplets:  $\mathcal{A}_f = D_f/H_f$ , where  $D_f$  and  $H_f$  are the final diameter and height, respectively. Figure 7(a,b) shows the variation of  $\mathcal{A}_f$  versus the Reynolds and Froude numbers, respectively. For a few data points, where  $Re$  and  $Fr$  are small, the aspect ratio is smaller than 1, i.e. only a small portion of the initially prolate droplet undergoes plastic deformation. For the pears and sombreros, increasing the inertial effects leads to a larger aspect ratio. For  $Re \lesssim 35$ , the data of all samples collapses with an almost linear dependence on  $Re$ . When plotted versus the Froude number, the values of the final aspect ratio depend on the rheology, for the same regime of low inertia: the softer the gel, the higher the aspect ratio. After reaching a maximum, the values of  $\mathcal{A}_f$  drop. This is when the regime transition to the bowl-shaped droplets occurs. The aspect ratio approaches unity (spherical

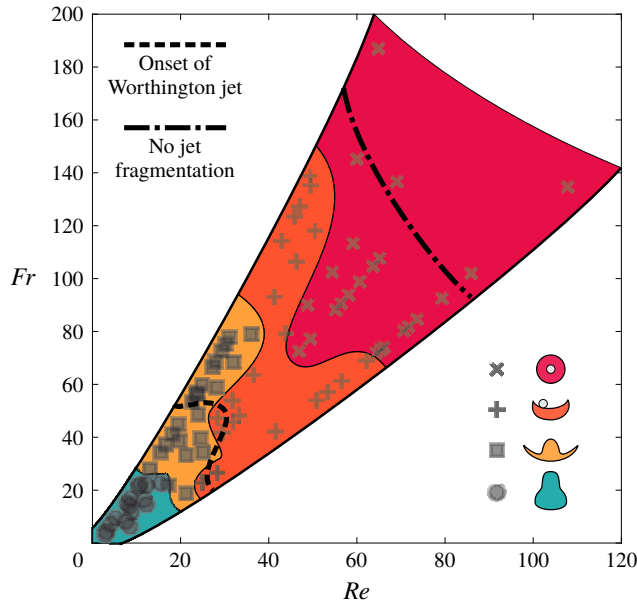


FIGURE 6. (Colour online) Different regimes of the final shapes. Symbols correspond to different shapes; see the legend.

capsules) with increasing inertial effects. Contrary to the previous two regimes, now the Froude number scales the data. We point out that the values of  $\mathcal{A}_0$  depend on the initial shape of the droplets (see figure 2c). Therefore we cannot make any scaling argument based on figure 7(a,b). We also look at the ratio of the final aspect ratio to the initial one,  $\mathcal{A}_f/\mathcal{A}_0$ . Similar to the trends of  $\mathcal{A}_f$ , the ratio initially increases with inertia (for pears and sombreros). The values drop when transitioning to the regime of bowl-shaped droplets. Interestingly, the final relative aspect ratio of the capsules (crosses in figure 7) seems to be only slightly dependent on the Froude number, reaching a universal value of  $\mathcal{A}_f/\mathcal{A}_0 \approx 3.2$ . The origin of this number, nonetheless, is not clear to us at this point. The values of the relative aspect ratio represent, to a degree, an efficiency factor of a water-entry system in deforming a viscoplastic droplet, where, for the regime of sombreros, it reaches values of as large as 10.

#### 4. Conclusion

In this paper, we have experimentally studied the water entry of a viscoplastic object. The system offers a method to sculpt the shape of droplets by merely making them pass through an air–water interface at different velocities. The problem shares characteristics with a classical water-entry problem of solid objects and the impact of immiscible droplets on a liquid surface. We show that the droplets reach the free surface with a static shape (balancing the capillary pressure and the yield stress), deform plastically upon entry (due to the shear stress and the motion of the cavity), and sink with a static shape at large time (balancing drag and gravity forces). The final shapes can be categorized using Reynolds and Froude numbers. By increasing these numbers, the shape of a viscoplastic droplet shifts from pears to sombreros to bowls, and eventually capsules. We categorize the final morphologies in a regime map and provide information on their final aspect ratio.

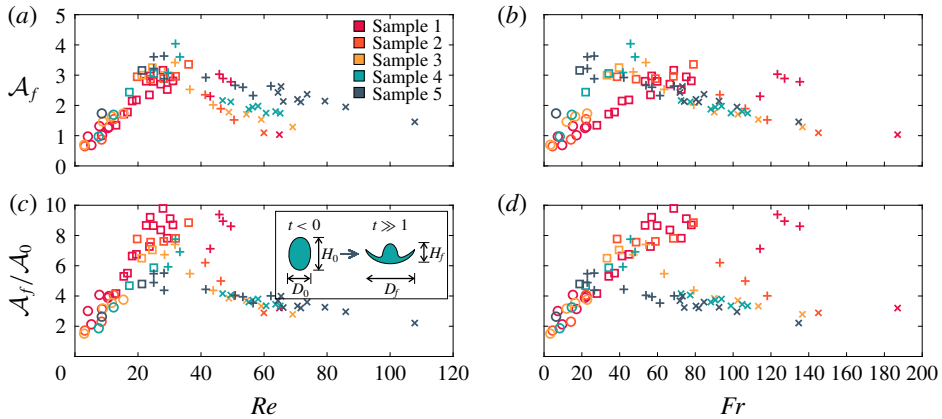


FIGURE 7. (Colour online) Final aspect ratio ( $\mathcal{A}_0 = D_0/H_0$ ) versus (a) Reynolds and (b) Froude numbers. Also, relative final aspect ratio ( $\mathcal{A}_f/\mathcal{A}_0$ ) versus (c) Reynolds number and (d) Froude number. Symbols represent different final shapes: pears (circles), sombreros (squares), bowls (pluses) and capsules (crosses). The inset in (c) shows the schematics of the initial and final shapes.

Our study has direct applications in non-spherical bead production. Additionally, among the final shapes, the production of capsules (especially if implemented on small scales) might be of particular interest for applications involving polymeric capsules such as controlled release of drugs, food additives and cell encapsulations (Zhang *et al.* 2006). In a broader perspective, the system provides information on the impact of elasto-plastic objects on water which has a wide range of applications in structure engineering (Peseux *et al.* 2005; Seddon & Moatamedi 2006). Finally, we would like to remark that more theoretical studies are required to explore many details of such a complicated system. An ideal model should involve a mathematical way to solve the moving boundaries of two deformable phases and incorporate the rheological properties. The development of such a model is currently work in progress.

### Acknowledgements

The authors thank C. Seyfert, D. van der Meer and A. Prosperetti for useful discussions.

### Supplementary movies

Supplementary movies are available at <https://doi.org/10.1017/jfm.2019.32>.

### Appendix A. First few moments

At the moment of impact, the bottom of the droplet experiences a sudden change of surrounding media, with a different density. This results in a shock-type pressure wave (water-hammer effect). Following the work of Miloh (1991), we can find an analytical expression for the small-time slamming coefficient:

$$C_S(t^*) = \frac{1}{2} F_S / (\rho_w \pi D_s^2 U_0^2) \approx 7.77 t^{*0.5} - 8.38 t^* - 12.05 t^{*1.5} + O(t^{*2}), \quad (\text{A } 1)$$

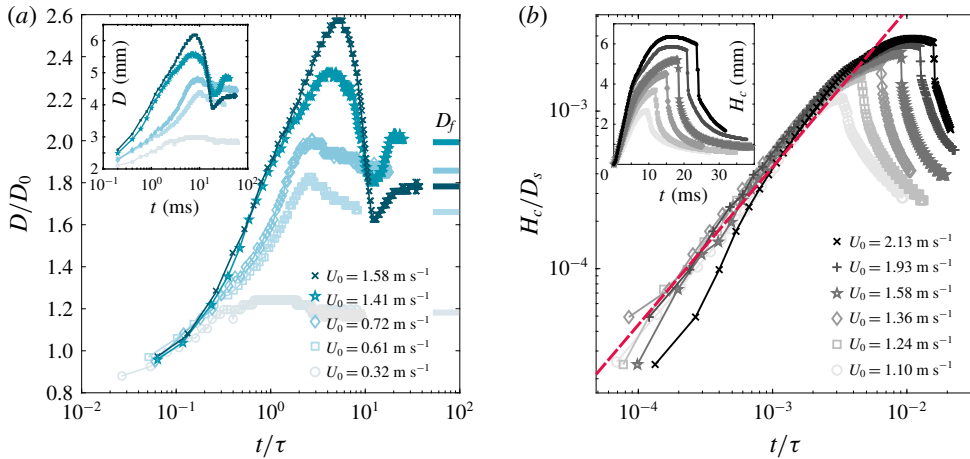


FIGURE 8. (Colour online) (a) Droplet diameter for sample 3 at different impact velocity. The inset is the same curve in a linear–linear scale. (b) Cavity maximum height for sample 2 at different impact velocity. The inset is the same curve in a linear–linear scale. The red dashed line in (b) shows  $H_c/D_s = 0.44t/\tau$ .

where  $F_S$  is the slamming force and  $t^* = t/\tau$ . Such analysis is common in slamming and water-entry processes to find the maximum shock pressure. Normalizing the slamming force with the effective area,  $A(t^*) = \pi D_s^2(t^* - t^{*2})$ , and the yield stress,  $\tau_0$ , leads to  $\mathcal{I}_{0+} = F_S/\tau_0 A$ . This  $\mathcal{I}_{0+}$  is singular at  $t = 0$ , as the magnitude of the slamming force decays much faster than the area, i.e. the slamming pressure is much larger than the yield stress at  $t = 0^+$ . The time scale of such phenomena is nonetheless small ( $D_s/c \sim O(10^{-6}$  s)), where  $c$  is the speed of sound in water. In our experiments, we did not see any effect of such pressure shock on the droplet.

## Appendix B. Dynamics

Figure 8 shows some qualitative analysis of what is explained in § 3.1. Figure 8(a) shows a series of examples of the temporal variation of the diameter of droplets of sample 3 at different impact velocities (only pears and sombreros are shown). In all cases, the droplet's diameter increases, almost linearly, reaching a maximum diameter at  $t/\tau \approx 3$ . The droplet then reaches an equilibrium diameter while it is elastically deforming. If the impact velocity is high enough, the brims of the sombreros elastically oscillate, as shown in § 3.1.

Figure 8(b) shows the evolution of the maximum height of the cavities for droplets of sample 2 at different impact velocities. Similar to figure 8(a), we exclude the bowls and capsules. The cavity height, at short time, grows linearly. The red dashed line denotes  $H_c/D_s = 0.44t/\tau$ , corresponding to the early-stage prediction of Bisighini *et al.* (2010), using an inviscid theory and ignoring the effects of gravity and droplet deceleration. After reaching a maximum value, the cavity retracts. The smaller the impact velocity, the smaller the cavity and the sooner it retracts.

## Appendix C. Very small and very large yield stress

The mechanics of viscoplastic water entry reported in the text change when the gel becomes very soft or very hard. By reducing the concentration of the polymer, we

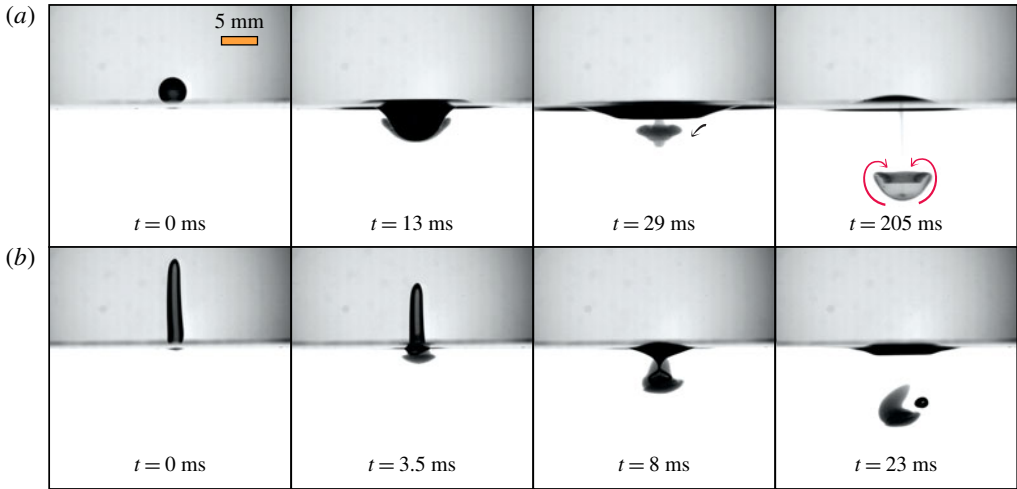


FIGURE 9. (Colour online) Impact of (a) a soft gel droplet ( $\tau_0 = 2$  Pa) at  $U_0 = 0.32$  m s $^{-1}$  and (b) a hard gel ( $\tau_0 = 35$  Pa) at  $U_0 = 0.65$  m s $^{-1}$ .

approach a Newtonian droplet. Figure 9(a) shows an example of water-entry process for a gel with  $\tau_0 \approx 2$  Pa at  $U_0 = 0.32$  m s $^{-1}$ . The droplet highly deforms at the early stage of the impact. Additionally, the motion of the free surface and the resultant fluid motion inside the bath significantly affect the shape of the droplet: the droplet first retracts with the cavity and later is pushed down ( $t = 29$  ms). Eventually, the vortex rings form and largely develop ( $t = 205$  ms). The yield stress only appears to be important at the late time when the sedimentation velocity and the flow around the droplet are small. Such a regime is close to impact of immiscible viscous droplets, previously studied by many (e.g. see San Lee *et al.* 2015; Thoraval *et al.* 2016).

Figure 9(b) shows an example of impact of a viscoplastic droplet of  $\tau_0 = 35$  Pa at  $U_0 = 0.65$  m s $^{-1}$ . The large yield stress results in a very small initial aspect ratio, which makes the experiments difficult. In several cases, the droplet already buckles during the formation (see Balmforth & Hewitt 2013). Also, a normal impact was hard to achieve, since the droplet tends to rotate before the impact. In a successful experiment, the tall droplets undergo buckling upon impact: the bottom of the droplet yields and deforms, and when the droplet is crossing the free surface, it bends. The process typically associates with bubble formation as well ( $t = 8$  ms).

## REFERENCES

- AUGUSTE, F., MAGNAUDET, J. & FABRE, D. 2013 Falling styles of disks. *J. Fluid Mech.* **719**, 388–405.
- BALMFORTH, N. & HEWITT, I. 2013 Viscoplastic sheets and threads. *J. Non-Newtonian Fluid Mech.* **193**, 28–42.
- BALMFORTH, N. J., FRIGAARD, I. A. & OVARLEZ, G. 2014 Yielding to stress: recent developments in viscoplastic fluid mechanics. *Annu. Rev. Fluid Mech.* **46**, 121–146.
- BESABATHUNI, S. N., LINDBERG, S. E., CAGGIONI, M., WESNER, C. & SHEN, A. Q. 2015 Getting in shape: molten wax drop deformation and solidification at an immiscible liquid interface. *J. Colloid Interface Sci.* **445**, 231–242.

- BERBEROVIĆ, E., VAN HINSBERG, N. P., JAKIRLIĆ, S., ROISMAN, I. V. & TROPEA, C. 2009 Drop impact onto a liquid layer of finite thickness: dynamics of the cavity evolution. *Phys. Rev. E* **79** (3), 036306.
- BERGMANN, R., VAN DER MEER, D., STIJNMAN, M., SANDTKE, M., PROSPERETTI, A. & LOHSE, D. 2006 Giant bubble pinch-off. *Phys. Rev. Lett.* **96** (15), 154505.
- BERGMANN, R., VAN DER MEER, D., GEKLE, S., VAN DER BOS, A. & LOHSE, D. 2009 Controlled impact of a disk on a water surface: cavity dynamics. *J. Fluid Mech.* **633**, 381–409.
- BINGHAM, E. C. 1917 An investigation of the laws of plastic flow. *Bull. Bur. Stand.* **13** (278), 309–353.
- BISIGHINI, A., COSSALI, G. E., TROPEA, C. & ROISMAN, I. V. 2010 Crater evolution after the impact of a drop onto a semi-infinite liquid target. *Phys. Rev. E* **82** (3), 036319.
- BLACKWELL, B. C., DEETJEN, M. E., GAUDIO, J. E. & EWOLDT, R. H. 2015 Sticking and splashing in yield-stress fluid drop impacts on coated surfaces. *Phys. Fluids* **27** (4), 043101.
- BONN, D., DENN, M. M., BERTHIER, L., DIVOUX, T. & MANNEVILLE, S. 2017 Yield stress materials in soft condensed matter. *Rev. Mod. Phys.* **89** (3), 035005.
- CAI, Y. 1989 Phenomena of a liquid drop falling to a liquid surface. *Exp. Fluids* **7** (6), 388–394.
- CHAPMAN, D. S. & CRITCHLOW, P. 1967 Formation of vortex rings from falling drops. *J. Fluid Mech.* **29** (1), 177–185.
- CHEN, S. & BERTOLA, V. 2017 Morphology of viscoplastic drop impact on viscoplastic surfaces. *Soft Matt.* **13** (4), 711–719.
- COUSSOT, P. 2014 Yield stress fluid flows: a review of experimental data. *J. Non-Newtonian Fluid Mech.* **211**, 31–49.
- DENG, Q., ANILKUMAR, A. & WANG, T. 2007 The role of viscosity and surface tension in bubble entrapment during drop impact onto a deep liquid pool. *J. Fluid Mech.* **578**, 119–138.
- DINGKREVE, M., PAREDES, J., DENN, M. M. & BONN, D. 2016 On different ways of measuring the yield stress. *J. Non-Newtonian Fluid Mech.* **238**, 233–241.
- DOOLEY, B. S., WARNCKE, A. E., GHARIB, M. & TRYGGVASON, G. 1997 Vortex ring generation due to the coalescence of a water drop at a free surface. *Exp. Fluids* **22** (5), 369–374.
- ELMORE, P., CHAHINE, G. & OGUZ, H. 2001 Cavity and flow measurements of reproducible bubble entrainment following drop impacts. *Exp. Fluids* **31** (6), 664–673.
- ESMAILIZADEH, L. & MESLER, R. 1986 Bubble entrainment with drops. *J. Colloid Interface Sci.* **110** (2), 561–574.
- FEDORCHENKO, A. I. & WANG, A.-B. 2004 On some common features of drop impact on liquid surfaces. *Phys. Fluids* **16** (5), 1349–1365.
- FRANZ, G. 1959 Splashes as sources of sound in liquids. *J. Acoust. Soc. Am.* **31** (8), 1080–1096.
- GERMAN, G. & BERTOLA, V. 2009 Impact of shear-thinning and yield-stress drops on solid substrates. *J. Phys.: Condens. Matter* **21** (37), 375111.
- GERMAN, G. & BERTOLA, V. 2010 The free-fall of viscoplastic drops. *J. Non-Newtonian Fluid Mech.* **165** (13), 825–828.
- GIELEN, M. V., SLEUTEL, P., BENSCHOP, J., RIEPEN, M., VORONINA, V., VISSER, C. W., LOHSE, D., SNOEIJER, J. H., VERSLUIS, M. & GELDERBLOM, H. 2017 Oblique drop impact onto a deep liquid pool. *Phys. Rev. Fluids* **2** (8), 083602.
- HALLETT, J. & CHRISTENSEN, L. 1984 Splash and penetration of drops in water. *J. Rech. Atmos.* **18** (4), 225–242.
- HERSCHEL, W. & BULKLEY, R. 1926 Measurement of consistency as applied to rubber–benzene solutions. *Proc. Am. Soc. Test. Mater.* **26**, 621–633.
- HSIAO, M., LICHTER, S. & QUINTERO, L. G. 1988 The critical Weber number for vortex and jet formation for drops impinging on a liquid pool. *Phys. Fluids* **31** (12), 3560–3562.
- HURD, R. C., BELDEN, J., JANDRON, M. A., FANNING, D. T., BOWER, A. F. & TRUSCOTT, T. T. 2017 Water entry of deformable spheres. *J. Fluid Mech.* **824**, 912–930.
- JALAAL, M. 2016 Controlled spreading of complex droplets. PhD thesis, University of British Columbia.

- JALAAL, M., BALMFORTH, N. J. & STOEBER, B. 2015 Slip of spreading viscoplastic droplets. *Langmuir* **31** (44), 12071–12075.
- JALAAL, M., SEYFERT, C., STOEBER, B. & BALMFORTH, N. 2018 Gel-controlled droplet spreading. *J. Fluid Mech.* **837**, 115–128.
- JALAAL, M. & STOEBER, B. 2014 Controlled spreading of thermo-responsive droplets. *Soft Matt.* **10** (6), 808–812.
- JØRGENSEN, L., LE MERRER, M., DELANOË-AYARI, H. & BARENTIN, C. 2015 Yield stress and elasticity influence on surface tension measurements. *Soft Matt.* **11** (25), 5111–5121.
- KOROBKIN, A. & PUKHNACHOV, V. 1988 Initial stage of water impact. *Annu. Rev. Fluid Mech.* **20** (1), 159–185.
- LEE, D., BEESABATHUNI, S. N. & SHEN, A. Q. 2015 Shape-tunable wax microparticle synthesis via microfluidics and droplet impact. *Biomicrofluidics* **9** (6), 064114.
- LENG, L. J. 2001 Splash formation by spherical drops. *J. Fluid Mech.* **427**, 73–105.
- LHUISSIER, H., SUN, C., PROSPERETTI, A. & LOHSE, D. 2013 Drop fragmentation at impact onto a bath of an immiscible liquid. *Phys. Rev. Lett.* **110** (26), 264503.
- LIOW, J.-L. & COLE, D. 2009 High framing rate PIV studies of an impinging water drop. In *28th International Congress on High-Speed Imaging and Photonics*, vol. 7126, p. 71260L. International Society for Optics and Photonics.
- LIU, Y. & DE BRUYN, J. R. 2018 Start-up flow of a yield-stress fluid in a vertical pipe. *J. Non-Newtonian Fluid Mech.* **257**, 50–58.
- LUSH, P. 1983 Impact of a liquid mass on a perfectly plastic solid. *J. Fluid Mech.* **135**, 373–387.
- LUU, L.-H. & FORTERRE, Y. 2009 Drop impact of yield-stress fluids. *J. Fluid Mech.* **632**, 301–327.
- MACKLIN, W. & METAXAS, G. 1976 Splashing of drops on liquid layers. *J. Appl. Phys.* **47** (9), 3963–3970.
- MADLENER, K., FREY, B. & CIEZKI, H. 2009 Generalized Reynolds number for non-Newtonian fluids. In *Progress in Propulsion Physics*, vol. 1, pp. 237–250. EDP Sciences.
- MANGLIK, R. M., WASEKAR, V. M. & ZHANG, J. 2001 Dynamic and equilibrium surface tension of aqueous surfactant and polymeric solutions. *Exp. Therm. Fluid Sci.* **25** (1), 55–64.
- MILOH, T. 1991 On the initial-stage slamming of a rigid sphere in a vertical water entry. *Appl. Ocean Res.* **13** (1), 43–48.
- MORTON, D., RUDMAN, M. & JONG-LENG, L. 2000 An investigation of the flow regimes resulting from splashing drops. *Phys. Fluids* **12** (4), 747–763.
- MURPHY, D. W., LI, C., D'ALBIGNAC, V., MORRA, D. & KATZ, J. 2015 Splash behaviour and oily marine aerosol production by raindrops impacting oil slicks. *J. Fluid Mech.* **780**, 536–577.
- OGUZ, H. N. & PROSPERETTI, A. 1990 Bubble entrainment by the impact of drops on liquid surfaces. *J. Fluid Mech.* **219**, 143–179.
- PECK, B. & SIGURDSON, L. 1994 The three-dimensional vortex structure of an impacting water drop. *Phys. Fluids* **6** (2), 564–576.
- PESEUX, B., GORNET, L. & DONGUY, B. 2005 Hydrodynamic impact: numerical and experimental investigations. *J. Fluids Struct.* **21** (3), 277–303.
- PETERS, I. R., VAN DER MEER, D. & GORDILLO, J. M. 2013 Splash wave and crown breakup after disc impact on a liquid surface. *J. Fluid Mech.* **724**, 553–580.
- PUMPHREY, H. C., CRUM, L. & BJØRNØ, L. 1989 Underwater sound produced by individual drop impacts and rainfall. *J. Acoust. Soc. Am.* **85** (4), 1518–1526.
- PUMPHREY, H. C. & ELMORE, P. A. 1990 The entrainment of bubbles by drop impacts. *J. Fluid Mech.* **220**, 539–567.
- KHALEEQ-UR RAHMAN, M. & SAUNDERS, C. 1988 Corona from splashing water drops. *J. Atmos. Terr. Phys.* **50** (6), 545–555.
- REIN, M. 1996 The transitional regime between coalescing and splashing drops. *J. Fluid Mech.* **306**, 145–165.
- ROBERTS, G. P. & BARNES, H. A. 2001 New measurements of the flow-curves for carbopol dispersions without slip artefacts. *Rheol. Acta* **40** (5), 499–503.
- SAN LEE, J., PARK, S. J., LEE, J. H., WEON, B. M., FEZZAA, K. & JE, J. H. 2015 Origin and dynamics of vortex rings in drop splashing. *Nat. Commun.* **6**, 8187.

- VAN DE SANDE, E., SMITH, J. M. & VAN OORD, J. 1974 Energy transfer and cavity formation in liquid-drop collisions. *J. Appl. Phys.* **45** (2), 748–753.
- SARAMITO, P. 2009 A new elastoviscoplastic model based on the Herschel–Bulkley viscoplastic model. *J. Non-Newtonian Fluid Mech.* **158** (1), 154–161.
- SEDDON, C. & MOATAMEDI, M. 2006 Review of water entry with applications to aerospace structures. *Intl J. Impact Engng* **32** (7), 1045–1067.
- SIGLER, J. & MESLER, R. 1990 The behavior of the gas film formed upon drop impact with a liquid surface. *J. Colloid Interface Sci.* **134** (2), 459–474.
- THOMPSON, R. L. & SOARES, E. J. 2016 Viscoplastic dimensionless numbers. *J. Non-Newtonian Fluid Mech.* **238**, 57–64.
- THOMSON, J. J. & NEWALL, H. F. 1886 V. On the formation of vortex rings by drops falling into liquids, and some allied phenomena. *Proc. R. Soc. Lond.* **39** (239–241), 417–436.
- THORAVAL, M.-J., LI, Y. & THORODDSEN, S. T. 2016 Vortex-ring-induced large bubble entrainment during drop impact. *Phys. Rev. E* **93** (3), 033128.
- TOMITA, Y., SAITO, T. & GANBARA, S. 2007 Surface breakup and air bubble formation by drop impact in the irregular entrainment region. *J. Fluid Mech.* **588**, 131–152.
- TRUSCOTT, T. T., EPPS, B. P. & BELDEN, J. 2014 Water entry of projectiles. *Annu. Rev. Fluid Mech.* **46**, 355–378.
- TRUSCOTT, T. T., EPPS, B. P. & TECHET, A. H. 2012 Unsteady forces on spheres during free-surface water entry. *J. Fluid Mech.* **704**, 173–210.
- WANG, T., LACÍK, I., BRISSOVÁ, M., ANILKUMAR, A. V., PROKOP, A., HUNKELER, D., GREEN, R., SHAHROKHI, K. & POWERS, A. C. 1997 An encapsulation system for the immunoisolation of pancreatic islets. *Nat. Biotechnol.* **15** (4), 358.
- WORTHINGTON, A. M. 1883 On impact with a liquid surface. *Proc. R. Soc. Lond.* **34** (220–223), 217–230.
- WORTHINGTON, A. M. 1908 *A Study of Splashes*. Longmans, Green.
- YARIN, A., RUBIN, M. & ROISMAN, I. 1995 Penetration of a rigid projectile into an elastic-plastic target of finite thickness. *Intl J. Impact Engng* **16** (5–6), 801–831.
- ZHANG, H., TUMARKIN, E., PEERANI, R., NIE, Z., SULLAN, R. M. A., WALKER, G. C. & KUMACHEVA, E. 2006 Microfluidic production of biopolymer microcapsules with controlled morphology. *J. Am. Chem. Soc.* **128** (37), 12205–12210.